SOFT ROBOTS

Variable-stiffness–morphing wheel inspired by the surface tension of a liquid droplet

Jae-Young Lee[1,2]†, Seongji Han[3,4]†, Munyu Kim[5], Yong-Sin Seo[1,2], Jongwoo Park[1], Dong Il Park[1], Chanhun Park[1], Hyunuk Seo[1], Joonho Lee[1], Hwi-Su Kim[1], Jeongae Bak[1], Hugo Rodrigue[2,6], Jin-Gyun Kim[3], Joono Cheong[5], Sung-Hyuk Song[1,7]*

Wheels have been commonly used for locomotion in mobile robots and transportation systems because of their simple structure and energy efficiency. However, the performance of wheels in overcoming obstacles is limited compared with their advantages in driving on normal flat ground. Here, we present a variable-stiffness wheel inspired by the surface tension of a liquid droplet. In a liquid droplet, as the cohesive force of the outermost liquid molecules increases, the net force pulling the liquid molecules inward also increases. This leads to high surface tension, resulting in the liquid droplet reverting to a circular shape from its distorted shape induced by gravitational forces. Similarly, the shape and stiffness of a wheel were controlled by changing the traction force at the outermost smart chain block. As the tension of the wire spokes connected to each chain block increased, the wheel characteristics reflected those of a general circular-rigid wheel, which has an advantage in high-speed locomotion on normal flat ground. Conversely, the modulus of the wheel decreased as the tension of the wire spoke decreased, and the wheel was easily deformed according to the shape of obstacles. This makes the wheel suitable for overcoming obstacles without requiring complex control or sensing systems. On the basis of this mechanism, a wheel was applied to a two-wheeled wheelchair system weighing 120 kilograms, and the state transition between a circular high-modulus state and a deformable low-modulus state was realized in real time when the wheelchair was driven in an outdoor environment.

INTRODUCTION

For robot or mobile systems to move on the ground without limitations related to terrestrial conditions, the ability to overcome obstacles has been a key function (*1*, *2*). Wheels are generally used to realize movement in robot or transporter systems and are among the oldest inventions in human history, but the wheel has limitations in overcoming relatively large obstacles, such as rocks or stairs. To increase the ability to overcome obstacles using wheels, articulated frames with multiple wheels, such as rocker-bogie mechanisms, have been developed (*3*–*6*), but the increases in the size and complexity of these systems are negative factors. The track-based locomotion system is a specially designed mechanism for uneven terrain based on increasing the contact area (*7*). However, the track-based system is limited by a relatively low speed and consumes more energy than wheeled systems because of the high friction from the increased contact area between the ground and system. In addition, vibration and friction can occur because of the discontinuous track profile with moving vertices and the difficulty of adapting the damping system (*8*). Leg-based locomotion systems have been adapted for structured environments and uneven terrain by mimicking the locomotion of animals or humans (*9*–*11*). This approach has the advantage of mimicking effective locomotion strategies in nature, such as the gait of cheetahs (*12*, *13*), dogs (*14*–*16*), horses (*17*), and humans (*18*–*23*). However, because of the complexity of these systems associated with the relatively large number of actuators and complex control systems, the energy efficiency of locomotion is relatively low, and it is difficult to realize such systems as the size and payload of the robot increase.

To overcome these limitations, hybrid locomotion systems that combine two or three different locomotion mechanisms have been proposed, such as leg-wheel, leg-track, wheel-track, and leg-wheel-track systems. (*7*). However, these combined locomotion mechanisms require complex mechanical and control systems (*24*–*28*), so it is difficult to establish reliable systems under unexpected, unstructured outdoor conditions without mechanical or control failure. As an alternative method, nonpneumatic tires have been developed to overcome the limitations of wheels. The nonpneumatic tire has an advantage in harsh driving conditions because it can prevent punctures, leaks, or blowouts, which cause critical safety issues; additionally, it can generate effective shock absorption with a high traction force because of the flexibility of the wheel (*29*, *30*). The performance of nonpneumatic tires mainly depends on the structural characteristics of the tires and the materials used and can be categorized as follows: multiple flexible spoke structures (*31*–*34*), multihole structures (*35*), mesh-like structures using spiral steel wire (*36*), shape-memory alloy structures (*37*), and deployable structures (*38*–*41*). However, the main purposes of these nonpneumatic tires are to prevent punctures and increase durability, not to overcome high obstacles. Therefore, the maximum deformable depth of the usual nonpneumatic tire is small to maintain driving stability on flat ground. As the overall stiffness of the nonpneumatic tire decreases, the available depth of deformation increases when in contact with the obstacle, and the ability to overcome the obstacle is enhanced. However, the moving speed and energy efficiency decrease in this case. Therefore, there is

---

[1] Advanced Robotics Research Center, Korea Institute of Machinery and Materials, University of Science and Technology, Daejeon 34103, Korea. [2] School of Mechanical Engineering, Sungkyunkwan University, Suwon 16419, Korea. [3] Department of Mechanical Engineering (Integrated Engineering), Kyung Hee University, Yongin 17104, Korea. [4] Department of Mechatronics Engineering, Chungnam National University, Daejeon 34134, Korea. [5] Department of Control and Instrumentation Engineering, Korea University, Sejeong 30019, Korea. [6] Department of Intelligent Robotics, Sungkyunkwan University, Suwon 16419, Korea. [7] Mechanical Engineering, School of Korea Institute of Machinery and Materials, University of Science and Technology, Daejeon 34103, Korea.
*Corresponding author. Email: shsong@kimm.re.kr
†These authors contributed equally to this work.

an inverse relationship between the ability to overcome obstacles and movement efficiency on flat ground, and it is challenging to optimize both simultaneously. In the case of the wheel using a deployable structure, the main purpose of applying this mechanism is to change the wheel size for adaptation to various obstacles (*38*, *39*), transform torque (*40*), and make efficient use of limited space (*41*). However, these transformable or deployable structures can only change the diameter of the wheel without varying the wheel stiffness, preventing the wheel from deforming to match the shape of obstacles for adaptation. Moreover, altering the wheel diameter poses challenges to the design of the integrated vehicle system because of the changing space requirements. In particular, when the diameter of the wheel increases, large vibrations can occur because of discontinuous sections in the structure, making it difficult to achieve stable movement at high speeds, which is a general advantage of wheels.

In this research, we propose a possible solution for this contradictory condition. Inspired by the surface tension of liquids, we present a method to adjust the stiffness and shape of wheels. Notably, the states of the wheel can be altered in real time between a rigid-circular–shape state for fast movement on flat ground and a soft-deformable state for overcoming obstacles. The rigidity of the wheel can be controlled by changing the tension of the wire spoke structure, which influences the surface tension of the smart chain structure located at the outermost edge of the wheel. When the wheel state changes to the fast movement mode, the surface tension of the wheel is increased by increasing the tension of the wire spoke structure, and then the shape of the wheel becomes circular and a high-rigidity state is achieved. On the other hand, when the wheel is in the obstacle-overcoming state because of decreased surface tension, it can easily deform to a depth of up to 40% of its radius. This liquid-mimetic variable-stiffness mechanism for adjusting the rigidity of the wheel helps to overcome the limitations of the wheel when obstacles are encountered while maintaining the original advantages of the wheel on flat ground. The basic characteristics and mechanism of the variable-stiffness wheel were verified, and an evaluation of its performance was conducted. A four-wheeled vehicle and a real-sized wheelchair system are proposed as possible applications of the surface-tension-mimetic variable-stiffness wheel.

RESULTS

Configuration of the variable-stiffness wheel inspired by the surface tension of liquid

To effectively overcome obstacles while maintaining the advantage of a general wheel driving on flat ground, a mechanism for realizing switchable wheel modes was proposed (Fig. 1A). When the wheel drives on a normal flat ground, it maintains a circular shape in a high-modulus state (Fig. 1Ai); thus, it functions as a normal wheel, displaying energy-efficient and stable movement during locomotion without shaking. When the wheel is used on rough terrain with large obstacles, where a typical wheel does not effectively function, the modulus of the proposed wheel decreases. This makes the wheel easily deformable, allowing it to adapt to the shape of the obstacle (Fig. 1Aii). The smart chain structure, which consists of a chain-like structure located at the outermost side of the wheel, is connected to a wire spoke structure (Fig. 1B). As shown by the green line in Fig. 1B, one wire is connected to one side of the chain block, passes through the hub structure colored in red in Fig. 1B, and is fixed to the opposite side of the chain block. The total length of the wire spoke structure is constant and equal to its total length in the initial configuration. Therefore, the length of the wire spoke from the chain block to the hub structure can be changed on the basis of the hub-gap distance between the front- and rear-hub structures (Fig. 1B). As the hub-gap distance increases to $l_{\mathrm{h\_large}}$, the length of the wire spoke between the chain block and hub structure decreases, and the chain block is forced inward. Then, the modulus of the wheel increases in a circular shape, and the wheel functions as a normal wheel (Fig. 1Ci). Otherwise, when the hub-gap distance decreases to $l_{\mathrm{h\_small}}$, the inward-directional force acting on the chain block also decreases. Then, the wheel enters a soft state, allowing it to deform effectively to adapt to the shape of the obstacle and overcome it (Fig. 1Cii).

The variation in stiffness is derived from the sum of the inward-directional force at the chain block, and it can be compared with the surface tension of a liquid droplet (Fig. 1D). The molecules located at the surface of a liquid are pulled inward because of the nonuniform cohesive forces, whereas the net force becomes zero for molecules inside the liquid. The sum of each cohesive force for the molecules at the surface can be described as the attraction force toward the center of the liquid. This attraction force can be matched to the force acting on the chain block because of the wire spokes in the wheel. As the length of a wire spoke from the chain block to the hub structure decreases at a large hub-gap distance, the force acting on the chain block can be separated into the tangential force that brings adjacent blocks closer to each other and the radial force that causes the blocks to move in the direction of the wheel center. This tangential force acting on the block is similar to the surface tension of a liquid, and the net force of each chain block plays a role in the contraction of the wheel structure and affects the shape and stiffness of the wheel. The dependence on contraction force on the variable stiffness of the wheel is similar to the dependence on surface tension on the variable contact angle of a liquid droplet (Fig. 1E). Because of the gravitational force, a liquid droplet is deformed at the surface, and this magnitude of deformation is generally represented as the contact angle. As the contact angle increases and approaches 180°, the shape of the liquid droplet approaches a circular shape with minimized deformation because of gravity. These shape variations of the liquid droplet depending on the surface tension are similar to the shape variations of the wheel depending on the surface tension controlled by the tension of the wire spoke structure.

Mechanism of stiffness variation for the proposed wheel

The smart chain structure is located above the soft supporting structure, which supports the initial position of the smart chain structure (Fig. 2A). The soft supporting structure can be replaced with any material or structure that is effective in realizing a large amount of deformation. The modulus of the soft supporting structure influences the range of stiffness variation of the wheel by varying the tension of the wire spoke. Individual smart chain structures are assembled by using a pin at the hole, similar to the method for assembling a general chain.

The stiffness of the wheel can be changed on the basis of two major mechanisms: the spoke length variation at the ground contact position and variation in the distance between each smart chain structure depending on the direction of rotation. In the case of the first mechanism, the required length of the spoke structure at the ground contact position increases as the depth of deformation increases. When the circular structure with radius R is pushed down to a distance d, which is defined as the depth of deformation (Fig. 2Bii),

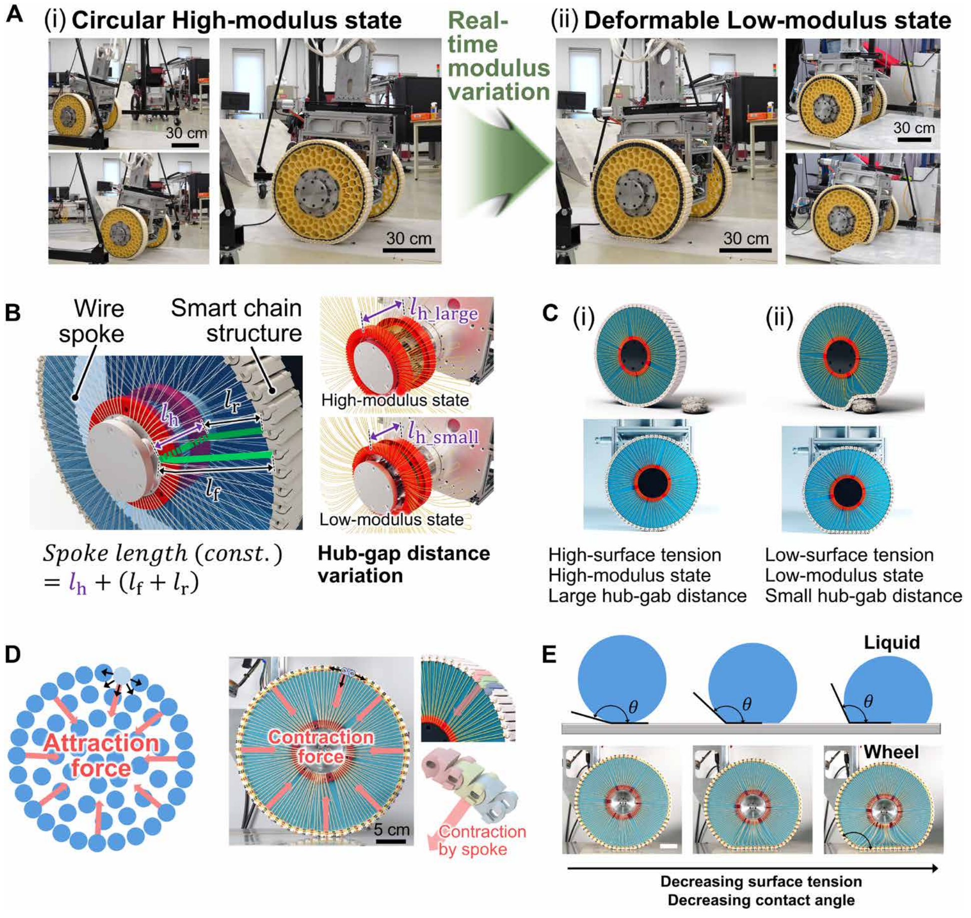

Fig. 1. Configuration of the variable-stiffness–morphing wheel. (**A**) State transition between the (i) circular high-modulus state and (ii) deformable low-modulus state of the wheel in the two-wheeled wheelchair system. (**B**) Configuration of the wire spoke and smart chain structure. The tension of the wire spoke can be varied by changing the distance between the hub structures. l_f indicates the spoke length on the front side of the wheel, and l_r indicates the spoke length on the rear side. (**C**) Description of wheel characteristics according to each state of the wheel [(i) circular high-modulus and (ii) deformable low-modulus states]. (**D**) Comparison between the attraction force of the liquid droplet and the contraction force in the wheel structure. (**E**) The similarity of shape variation depends on the surface tension of the liquid droplet and the wheel. Scale bar, 5 cm.

the point P_{int} at which the wheel touches the ground and begins to bend away from the ground occurs. Then, l_o is defined as the outer length of the overlapped part of the circular structure with the ground. If the circumference of the circular structure is constant and if there is no wrinkling or partial roll-up, then the contact length between the ground and circular structure becomes not l_o, which is the intersected length of the line where they overlap, but l_o (Fig. 2Biii). The increased contact length between the circular structure and ground, from l_o', is given by $2\Delta l_o$, where

$$\Delta l_o = \frac{l_o - l_o'}{2} = R\cos^{-1}\left(1-\frac{d}{R}\right) - \sqrt{2Rd-d^2} \qquad (1)$$

Consequently, the position where the wheel begins to bend away from the ground changes from P_{int} to P_d, which is shown as a red line in Fig. 2Biii. The distance variation between the center of the circular structure and P_d is R', so the length of the wire spoke of the wheel needs to increase with ΔR as follows

$$\Delta R = R' - R = \sqrt{\left[R\cos^{-1}\left(1-\frac{d}{R}\right)\right]^2 + (R-d)^2} - R \qquad (2)$$

The ΔR value generally increases as the depth of deformation d increases until $d < R$, which means that the maximum elongated length of the wire spoke influences the depth of deformation d on flat ground. If the circumference of the circular structure consists of a block with a thickness t (Fig. 2C), then the rotation center of each block is determined by the way that the blocks are assembled and how they contact each other. The center of rotation of the block can be located at its middle (Fig. 2C), meaning that each block is assembled using a pin at the middle of the block relative to the block thickness. Otherwise, this center of rotation can be located at the top or bottom side of the block (fig. S1). When the depth of deformation d is reached, the overlapped length of the middle line of the block, which is also the line of the neutral axis of deformation, is defined as l_m (Fig. 2Cii). Similar to Fig. 2B, the contact line between the ground and the wheel increases from l_m' by $2\Delta l_m$ (Fig. 2Ciii); thus, the length of the wire spoke of the wheel needs to increase to R' by ΔR, as shown in Eq. 2. In this case, the thickness of block t does not affect ΔR. When the rotation center of a block is at the top or bottom side (fig. S1), it is similar to a block rolling against the surface of another block. Therefore, each block cannot be overlapped with each other (fig. S1iii). In this case, the contact length (l_s') is increased by $2\Delta l_{s\_1}$, which is given by

$$\Delta l_{s\_1} = \left(R+\frac{t}{2}\right)\cos^{-1}\left(1-\frac{d}{R}\right) - \sqrt{2Rd-d^2} \qquad (3)$$

The length of the wire spoke needs to be increased by ΔR_1 as follows

$$\Delta R_1 = R' - R = \sqrt{\left[\left(R+\frac{t}{2}\right)\cos^{-1}\left(1-\frac{d}{R}\right)\right]^2 + (R-d)^2} - R \qquad (4)$$

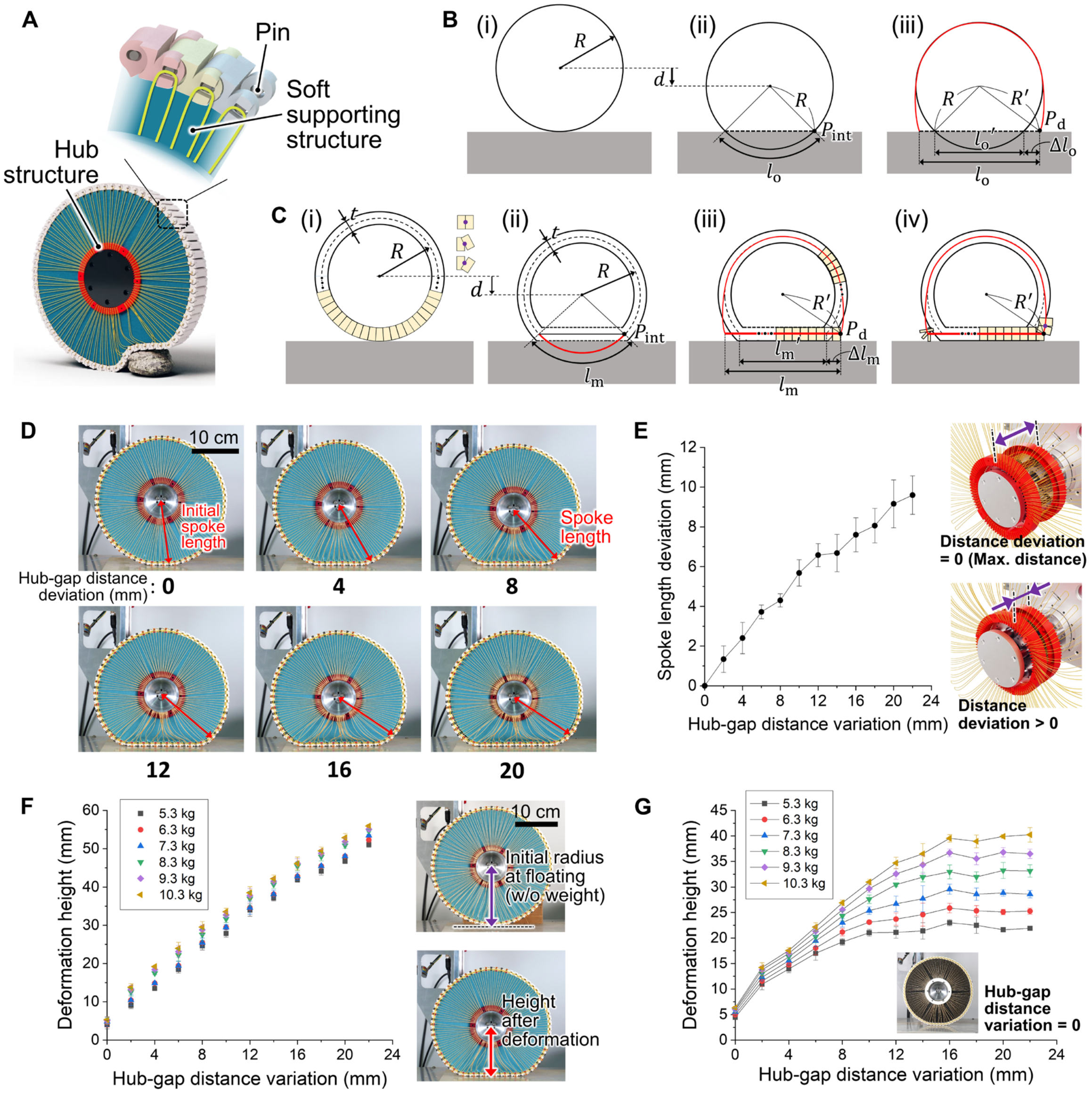

Fig. 2. Stiffness-variation mechanism based on the tension of the wire spoke structure. (**A**) Configuration of the soft supporting structure and the pin in the smart chain block. (**B**) Diagram of the simplified one-dimensional wheel model showing the effect of the length of the wire spoke. (**C**) Diagram of the simplified two-dimensional wheel model showing the effect of the length of the wire spoke. (**D**) Shape of the deformed wheel considering that the gravitational force depends on the hub-gap distance variation. (**E**) Measured length of the wire spoke at the deformed position from the ground based on the hub-gap distance variation. Error bars represent SD ($n = 5$). The deformation height of the wheel based on the hub-gap distance variation achieved with (**F**) a blue sponge or (**G**) a black sponge as the soft supporting structure. Error bars represent SD ($n = 3$).

In addition, the block next to that contacting the surface starts to separate from the ground (marked in green in fig. S1iv), and the required length of the wire spoke is increased from R' by ΔR_2, expressed as

$$\Delta R_2 = R'' - R' = \sqrt{\left(\frac{t}{2}\sin\theta + \frac{l_s}{2}\right)^2 + \left[R - d - \frac{t}{2}(1-\cos\theta)\right]^2} - R' \tag{5}$$

where θ is the angle of the deformed block from the ground, and the wire spoke is assumed to be connected to the middle of the block at P_{d_2}. Each block is rotated about the edge of the block marked with a purple dot; then, l_s is increased by $2\Delta l_{s\_2}$. Therefore, the required length of the wire spoke at the given depth of deformation is affected by the thickness of block t and the angle of block deformation θ, unlike in the case in Fig. 2C. Because of this complex and sensitive effect on the variation in the length of the wire spoke, we established the rotation axis near the center of the block, similar to that shown in Fig. 2C, not at the edge of the block. As a result, the deformation height of the wheel with a 140-mm radius in Fig. 2D can be controlled by varying the spoke length where the block begins to bend away from the ground, marked as point P_d in Fig. 2C. The maximum length of the wire spoke can be controlled on the basis of the deviation in the hub-gap distance, and, therefore, the length of the wire spoke near position P_d can be controlled on the basis of the hub-gap distance. The longest measured value among the length of wire spoke obtained near point P_d was used as a standard in Fig. 2E; this ambiguity arises from the discontinuity of the chain block and difficulties in distinguishing where the slope changes. The hub-gap distance variation was defined as zero when the distance reached a maximum in the initial state, and the distance variation values increased as the hub structures moved closer together (Fig. 2E). The spoke length deviation was derived from the difference between the length variation of the wire spoke and its initial length when the hub-gap deviation is zero. Because of the length variation of the wire spoke associated with the variation in hub-gap distance, the deformation height of the wheel can be changed (Fig. 2F). After the hub-gap distance reached the target value, the wheel was placed on the ground, and it started to deform until reaching an equilibrium position because of the gravitational force. Thus, the deformation height was defined as the deviation between the initial radius of the wheel in the floating state in air without the tension of the wire spoke and the current height of the wheel center after deformation (Fig. 2F). The deformation height was mainly influenced by the hub-gap distance, not by the dead weight applied to the wheel. This is because the soft supporting layer of the wheel in Fig. 2F was sufficiently soft. Thus, the magnitude of wheel deformation, controlled by the hub-gap distance, reached its limit before the soft supporting structure reached its equilibrium position because of the reaction force generated by the deformation. If the value of the applied dead weight was lighter than the experimental values, then the effect of the soft supporting structure became dominant. Consequently, the deformation height of the wheel reached its maximum when the soft supporting structure had sufficiently deformed and before the limit position controlled by the hub-gap distance. In other words, the effect of the soft supporting structure became dominant as the relative modulus of the soft supporting structure increased compared with that for an applied gravitational force.

The deformation height was measured using the wheel model with a soft supporting structure of higher modulus (the moduli of the soft supporting structures in Fig. 2, F and G, are presented in fig. S2), as shown in Fig. 2G, to verify the effect of the relative modulus of the soft supporting structure. When the hub-gap distance variation was near zero, the effect of the external gravitational force became negligible for different deformation heights. This means that the variation in surface tension because of the hub-gap distance primarily affected the characteristics of the wheel when in a high–surface tension state. As the hub-gap distance variation increased, the influence of the applied weight became dominant for the deformation height, whereas the influence of the hub-gap distance variation itself on the deformation height decreased. This is because the possible range of deformation height was controlled by the hub-gap distance, but the deformation of the soft supporting structure reached an equilibrium position as the reaction force increased from deformation, even before the maximum deformation height was attained. These trends can be observed in fig. S3. As the hub-gap distance variation decreased, the deformation heights of each wheel using different soft supporting structures became similar. This is because the influence of surface tension became more dominant as the hub-gap distance variation decreased. Conversely, as the hub-gap distance variation increased, the differences in deformation height between the wheels with different soft supporting structures became more noticeable. To verify the effect of distance variations during the deformation process, the distance variations from the wheel center to each block were measured while the wheel was slowly placed on the ground from the floating state (fig. S4) at a fixed hub-gap distance. As the magnitude of deformation increased, the distance of the blocks located right below the wheel center, such as block numbers 16 and 18, decreased (fig. S4B), whereas the distance of the blocks located at the section where the blocks were bent and moved away from the ground increased. In particular, the distance of block number 22 rapidly increased as it approached the available maximum deformation (fig. S4C). This is because the position of block 22 was the nearest position at which the block was lifted from the ground when the wheel deformation reached a maximum for the given hub-gap distance conditions.

The second main mechanism that controls the stiffness of the wheel is the variation in the distance between each chain structure. The proposed smart chain structure was designed to have different distances between each block depending on the direction of rotation (Fig. 3). When the block rotates in the negative direction, where the largest deformation occurs in the inward direction (marked by the red circle in Fig. 3A) as the edges of obstacles are encountered, the distance between each block remains constant, but the angle of rotation increases. This movement direction was defined as the direction of negative curvature, and the contact surface between each smart chain structure was a circular shape in this direction. On the other hand, on the basis of the position at which concentrated and large inward directional deformation occurred, the smart chain block rotated in the positive direction near both sides of the wheel (marked by the green circle in Fig. 3A) as the distance between each block increased. This characteristic is because of the specially designed external shape of the smart chain block. On the upper side of the chain block, there is a small bump that alters the distance as the block rotates in the positive direction. As the angle of rotation increased, each block in the contact state continued to follow the protrusion path, and then the distance between each block increased. The pins are located at the hole in each smart chain structure to prevent the blocks from being disassembled (Fig. 3B). The hole shape is elliptical, and the pin can freely move in the lateral direction. When the block rotated in the direction of positive curvature, the distance between each block increased until the pin was stuck in the reduced volume of the overlapping area of pin holes of each block. For rotation in the direction of negative curvature, the distance between each block was maintained because the rotation axis of each block coincided with a circular shape. If a block rotated more than 90°, then the pin prevented further rotation because of the increased distance between each block. Therefore, the pin and the shape of the hole determined the range of rotation of each block.

This distance variation of the block mechanism was applied because of the different physical characteristics of a liquid droplet and a wheel. In the case of a liquid droplet, its total volume is conserved even when the shape of the liquid droplet changes, whereas the volume of the soft supporting structure in the wheel can be compressed, and the total volume of the wheel was decreased when an inward directional force was applied to the wheel. Because of these factors, the principle associated with the minimization of the surface area for a given volume in a liquid droplet because of surface tension, which is the reason liquid droplets have a spherical shape, was not applied to the wheel. However, if the distance between each block was changed depending on the rotation conditions, then the total surface area (or total length of the wheel circumference) was changed.

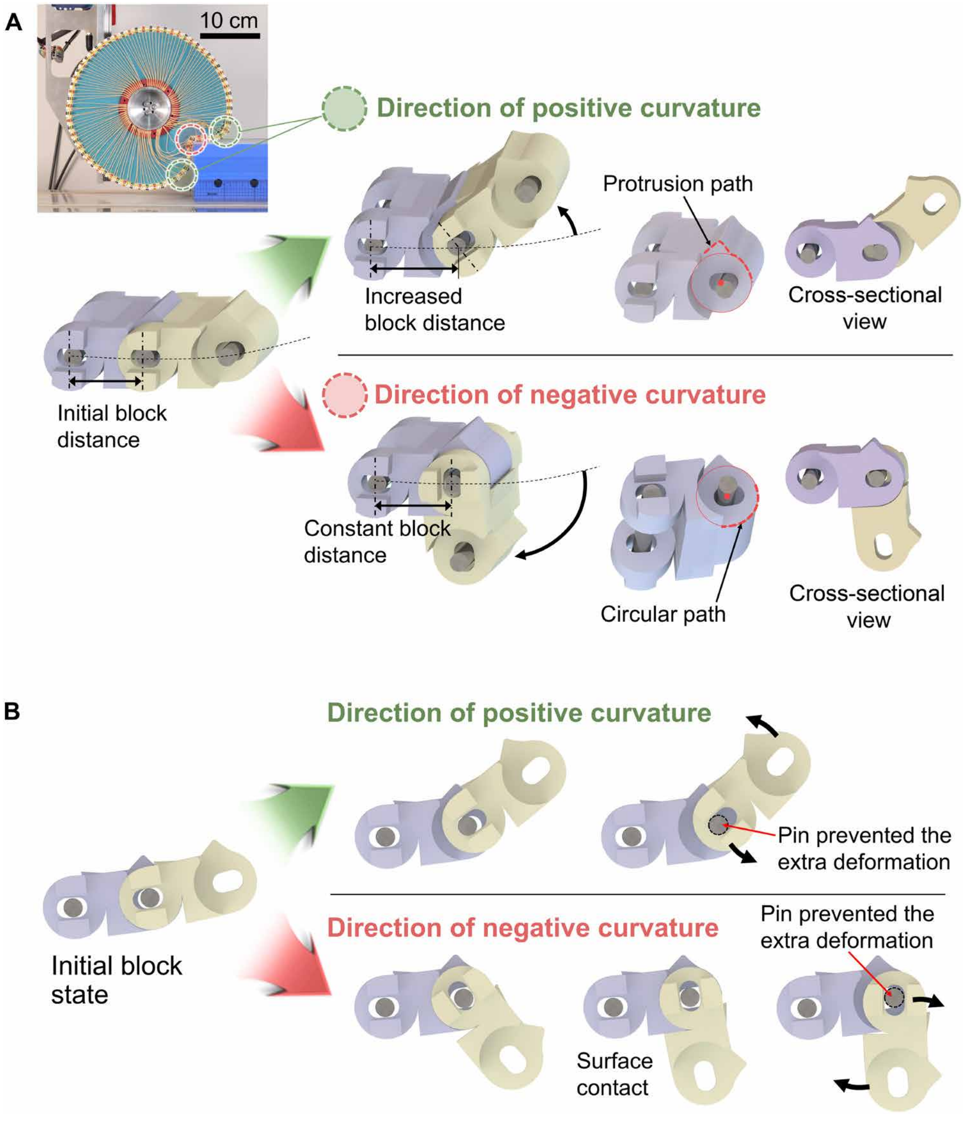

Fig. 3. Geometrical description of the smart chain structure. (**A**) The relative distance variation between each block depends on the direction of curvature. (**B**) The role of the pin in the chain block in the direction of positive or negative curvature.

Therefore, the potential energy derived from the contraction force of a wire spoke was not minimized when the total surface area increased because of the rotation of the blocks. This was comparable to a liquid that shows minimum potential energy at the minimum surface area. The shape of the smart chain structure was designed to minimize the wheel circumference when the wheel was circular. If any deformation started to occur from the initial circular shape, then the direction of positive curvature was generated as a result, leading to an increase in the total potential energy. For example, when concentrated inward directional deformation occurred (fig. S5), the chain block, situated relatively close to both sides from the position where the concentrated deformation occurred, rotated in the positive direction. Therefore, the total potential energy increased as the length of the circumference increased. The effect of the distance variation of each block was measured as deformation occurred at the fixed hub-gap distance (fig. S6). The wheel was slowly placed on the ground from the floating state, and the total length of the blocks was measured by adding the individual distance between each block. As a result, the total length of the blocks decreased as the center displacement increased until the wheel reached the state of maximum possible deformation. This is because the blocks are partially separated from each other when the wheel floats without an external load; then, the blocks were pushed close to each other as the center displacement increased. These gaps between blocks were diminished after 20 mm of center displacement, and the total length was maintained at a constant thereafter. When the wheel deformation approached its maximum value, the blocks located around the position where the wheels deformed in the direction away from the ground were deformed in the direction of positive curvature, so the distance between the blocks increased.

In a situation in which the wheel was pressed against an obstacle, negative curvature was generated where the largest deformation occurred at the edge of the obstacle, and positive curvature was generated at the same time; thus, the total length of the blocks increased (fig. S7). The magnitude of curvature because of adaptation to the obstacle increased as the deformation distance, which was defined from the wheel center to the edge of the obstacle, increased. As a result, the total length variation increased as the depth of deformation increased (fig. S7C). To verify the effects of distance variation on the basis of the rotation angle and direction in detail, the distance between each adjacent individual block was measured on the basis of the relative rotation angle between each block (fig. S8).

Evaluation of the variable stiffness of the proposed wheel

To evaluate the dependence of stiffness variation on the hub-gap distance, the wheel with a 140-mm radius was installed in the experimental setup (Fig. 4A). Different sizes of indenters could be installed in the experimental setup, and the reaction force associated with each indenter was measured while the indenter was transferred downward. The indenter with a wide shape was used to mimic the scenario in which the wheel was at rest on typical flat ground. The indenter with a narrow shape was used to mimic the scenario at which the wheel was deformed by an obstacle, similar to applying a concentrated force associated with encountering an obstacle. First, the reaction force was measured with the wide-shaped indenter. The reaction force displayed a different trend before and after a 4-mm hub-gap distance variation was reached (Fig. 4B). When the hub-gap distance variation was smaller than 2 mm, the force-displacement slope changed, with ~1.5 mm of displacement (Fig. 4C); then, the

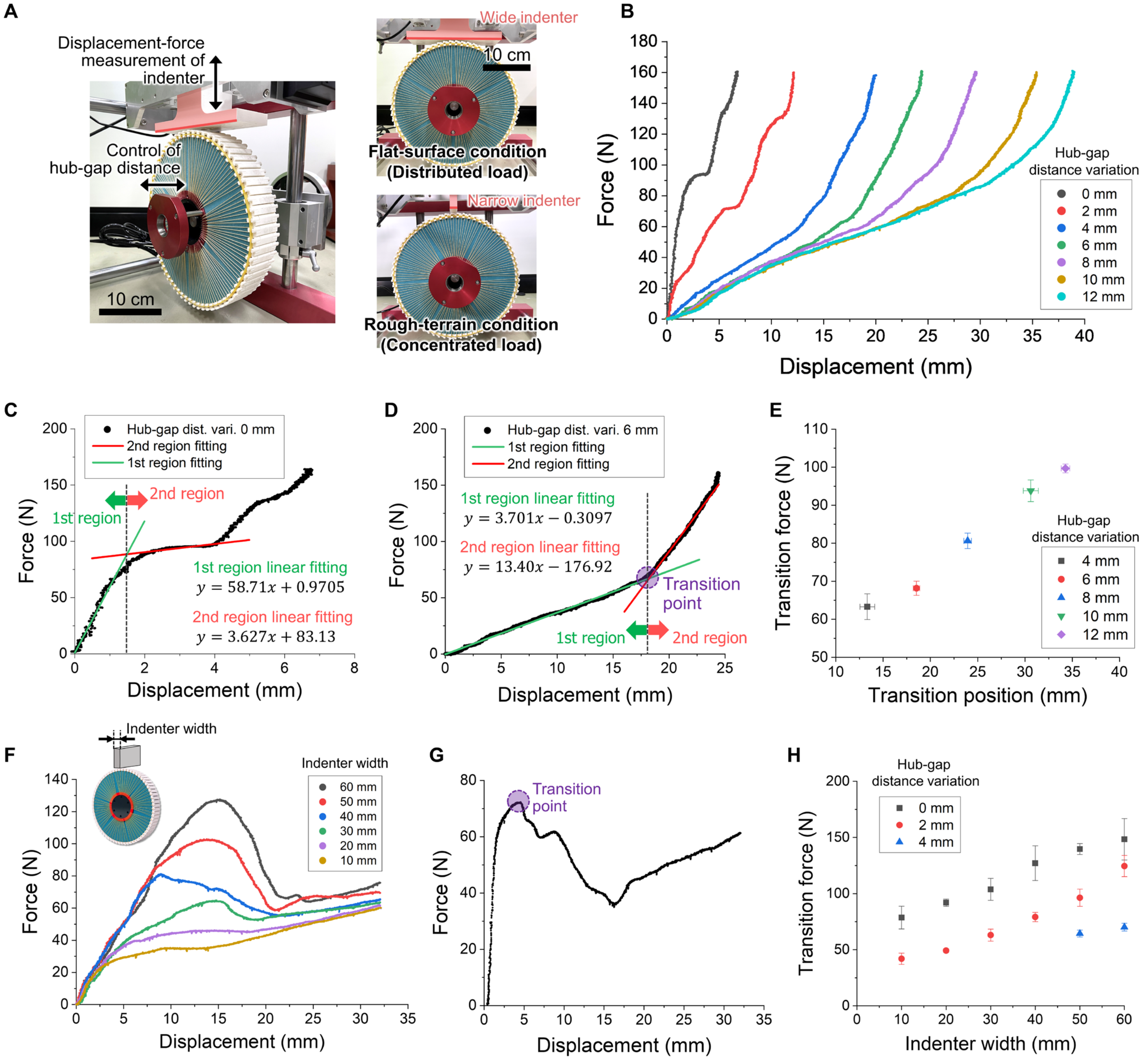

Fig. 4. Evaluation of wheel characteristics based on the surface tension. (**A**) Experimental setup for evaluating basic wheel characteristics. (**B**) Required force to generate deformation at each displacement on the basis of the hub-gap distance variation. The required force is measured as the change in deformation displacement when the hub-gap distance variation is fixed at (**C**) 0 mm or (**D**) 6 mm. Fitting lines in (C) and (D) were derived by linearly fitting the measured data in each region, except for the values at the transition position. (**E**) The analyzed transition force and transition displacement position depend on the hub-gap distance variation. Error bars represent SD ($n = 3$). From (B) to (E), the wide indenter was used to simulate flat ground. (**F**) Required force to generate deformation at each displacement on the basis of the variation in the indenter width. The hub-gap distance variation was fixed at 2 mm. (**G**) Measured reaction force based on displacement with a 10-mm-wide indenter and 0-mm hub-gap distance variation. (**H**) Transition force at each indenter width based on the hub-gap distance variation. Error bars represent SD ($n = 3$).

first part of the graph can be divided into two regions: the first region of high stiffness and the second region of low stiffness. The first region represents the normal state in which the wheel maintains its circular shape in a stable manner. When the applied pressure became larger than the boundary value of the first region, the chain block structure of the wheel that was in contact with the ground was partially buckled inward, and the second region was reached. When the hub-gap distance variation was larger than 4 mm, the characteristics of the wheel differed compared with those at 0-and 2-mm hub-gap distance variations. The stiffness of the wheel was lower in the first region and higher in the second region after the transition point was reached (Fig. 4D). When a force started to be applied to the wheel, the soft supporting structure started to deform until the desired deformation height was reached at the given hub-gap distance. After the wheel reached its desired deformation height, the tension of the wire spoke structure started to rapidly increase because of the mechanism shown in Fig. 2C, and then the stiffness of the wheel increased, as shown in the second region. Because of the dominant role of the wire spoke structure at the transition point, the hub-gap distance mainly influenced the required displacement and force at the transition position (Fig. 4E). In addition, as the hub-gap distance variation increased, more deformation was required before the stiffness started to increase substantially. The force required to maintain each hub-gap distance was measured as shown in fig. S9.

In the case of using a narrow shape indenter, a concentrated applied force on the wheel was generated, which was similar to the deformation of the wheel when pressing against obstacles (Fig. 4F). By decreasing the width of the indenter, situations in which the wheel overcomes sharp obstacles could be simulated. As the deformation magnitude from displacement of the indenter increased, the transition point at which the slope started to decrease was observed. The position of the transition point was shifted to a larger deformation value as the width of the indenter increased, and the slope before the transition point was maintained. Because of the decreasing modulus of the wheel after the transition point, the wheel was easily deformed, with potentially large deformations, according to the shape of the obstacle. This trend is shown in Fig. 4G. As the hub-gap distance increased, the force required to reach the transition position decreased for the same indenter width (Fig. 4H and fig. S10). When the hub-gap distance variation was 4 mm, the transition point appeared when the width of the indenter was more than 50 mm.

Evaluation of the wheel overcoming obstacles

To evaluate the ability of the wheel to overcome obstacles, the trajectory of the wheel was measured for an obstacle with a square shape. As the hub-gap distance variation increased, the position of the center of the wheel lowered because of the decreasing modulus of the wheel (Fig. 5A). In particular, when the hub-gap distance variation was less than 4 mm, the position of the center of the wheel was higher compared with cases with larger hub-gap distance variations, because the wheel shape was relatively circular without deformation from gravitational force. However, because of the increased stiffness, the wheel was difficult to deform to the shape of the obstacle. Therefore, the wheel could not overcome the obstacles when the hub-gap distance was less than 4 mm. When the wheel moved down a step, the trajectory for a hub-gap distance variation of 0 mm was similar to that for a wheel with a rigid-circular shape, as the wheel rotated around the edge of the step as the rotation axis (Fig. 5B). When the hub-gap distance variation was larger than 2 mm, deformation occurred as the wheel approached the edge of the step. As the wheel approached the edge of the step, the magnitude of the radial directional force on the wheel from the obstacle increased. Consequently, the distance between the edge of the step and the starting position of the deformation increased as the hub-gap distance variation increased. The gravitational force from the additional weight affected the depth of deformation at the obstacle (fig. S11A), and these variables were proportional to each other. However, until the wheel made contact with an obstacle, its height remained nearly constant regardless of the weight. This finding means that, after the deformation caused by an obstacle, the stiffness of the soft supporting structure predominantly affected the characteristics of the wheel. Therefore, the stiffness of the soft supporting structure needs to be relatively high to maintain a similar shape of deformation under high payload conditions (figs. S11B and S12).

The real-time variation in stiffness required to overcome an obstacle was implemented in the proposed wheel (Fig. 5C and movie S1). As an example of ascending motion, the wheel could maintain a circular high-modulus state before contact with an obstacle; then, the modulus of the wheel decreased to achieve an easily deformable state. After climbing on the step and overcoming obstacles, the wheel returned to the high-modulus state. This process could be repeated in descending motion to minimize abrupt *z*-directional acceleration. If the wheel maintained the high-modulus mode during its descending motion, then the contact area between the wheel and the step obstacles was limited only to the edge of the step. This limitation reduced the stability of the wheel. The high *z*-directional acceleration because of the rotation axis at the edge of the obstacle, which was evident from the steeper slope of the trajectory just before the wheel contacted the ground, also negatively affected stable locomotion (Fig. 5C). The height of the wheel could also be controlled by continuously changing the modulus of the wheel in real time (Fig. 5D, fig. S13, and movie S2).

The ability to overcome obstacles was mainly affected by the hub-gap distance variation, such as the height of obstacles (Fig. 6). The stability of climbing was defined as follows

$$\text{Stability} = \frac{l_{\text{block}}}{d_{\text{slip}} + l_{\text{block}}} \tag{6}$$

where l_{block} is the length of the unit smart chain block and d_{slip} is the slip distance at which the wheel slides off the ground before starting to climb the step-shaped obstacle. As the stability value approached 1, the slip distance decreased, and then the wheel climbed the obstacle in a stable manner. As the hub-gap distance variation increased, the decreased wheel modulus allowed the wheel to stably climb higher step-shaped obstacles (Fig. 6A). However, when the hub-gap distance variation exceeded a certain value and the step height was higher than 100 mm, the stability decreased because of the relatively low height of the wheel before the wheel contacted the obstacle. When the weight applied to the wheel increased, the hub-gap distance variation needed to be increased for stable climbing (Fig. 6B). When the hub-gab distance variation was small, the deformation generated in the wheel from the obstacle was not completely restored after overcoming the obstacle (fig. S14). This characteristic could be minimized by using a high-modulus soft supporting structure (fig. S15). The average traction force of the wheel was measured as 23.4 N with a 5.3-kg applied weight and 32.7 N with a 7.3-kg applied weight (fig. S16). Under high-speed driving conditions, the vibration characteristics of the wheel, using two different soft supporting structures, were evaluated on the basis of changes in the hub-gap distance variation (figs. S17 to S20 and movie S3). Regarding durability, the tensile strength of the single wire spoke module was also measured, and its average value was 1.193 kN (fig. S21).

In the simulation results, the trajectories of the wheel when ascending and descending step-shaped obstacles displayed characteristics similar to those in the experimental results (Fig. 6, D and E, and movie S4). The detailed shape of deformation (Fig. 6F) and the position variation of each chain block (fig. S23 and Supplementary Methods) were also verified. In addition, the state transition between the circular high-modulus and deformable low-modulus

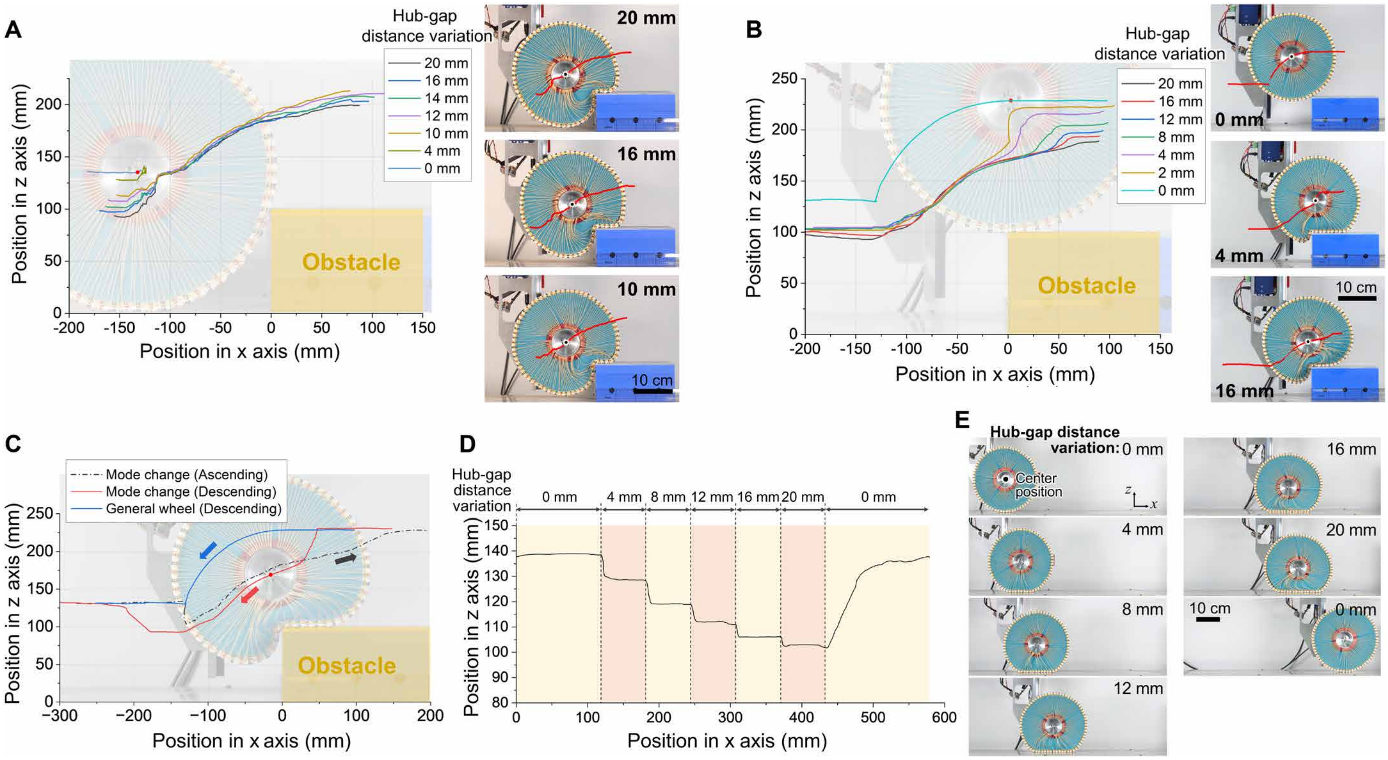

Fig. 5. Evaluation of wheel trajectory. (**A**) The trajectory of the center of the wheel based on the hub-gap distance variation when the wheel ascends a step-shaped obstacle. (**B**) The trajectory of the center of the wheel based on the hub-gap distance variation when the wheel descends a step-shaped obstacle. (**C**) Trajectory of the center of the wheel while ascending and descending a step-shaped obstacle and experiencing state transitions. The blue line represents the descending trajectory of the wheels, similar to that of a normal rigid circular wheel, which is simulated with a 0-mm hub-gap distance variation. (**D**) The position of the wheel center depends on the hub-gap distance and (**E**) the deformed shape of the wheel when the wheel moves on a flat surface.

states was verified in the simulation (fig. S24 and Supplementary Methods).

Demonstration in a vehicle system

A variable-stiffness wheel was implemented in a four-wheeled vehicle system for performance evaluation (Fig. 7, A and B; movie S5; and fig. S25). The surface tension of all four wheels could be adjusted individually, and a black sponge was used as the soft supporting structure because of the increased weight of the system. The four-wheeled vehicle system could operate with wheels in a circular high-modulus state on flat ground, and the vehicle could overcome rocks with irregular shapes by transitioning the wheels to the deformable low-modulus state (Fig. 7A). In a similar sequence, the four-wheeled vehicle could overcome a 180-mm-high obstacle, which was 1.2 times higher than the wheel radius (Fig. 7B).

The wheel was also implemented in a two-wheeled wheelchair system (fig. S26). In this case, the size of the wheel was doubled, considering the size of the wheelchair user. The weight of the vehicle system was ~120 kg, which was four times heavier than the weight of the four-wheeled system. Because the sponge structure had limitations in terms of increasing stiffness, a urethane honeycomb structure was applied as the soft supporting structure. The traction force (fig. S27) and the vibration characteristics of the large-sized wheel were evaluated at high speeds of up to 30 km/hour (fig. S28 and movie S6), and its durability was also tested for more than an hour at a speed of 15 km/hour (movie S7). The dynamics of the two-wheeled wheelchair system was studied (Supplementary Methods), and a control algorithm was developed (Supplementary Methods). The resulting control input torque applied to the wheelchair can be described as

$$\begin{aligned}\tau(t) &= \tau_{\mathrm{ffw}}(t)+\tau_{\mathrm{fdk}}(t)\\ &= Y^{\dagger}\left[M\left(q_d(t)\right)\ddot{q}_d(t)+N\left(q_d(t),\dot{q}_d(t)\right)+G\left(q_d(t)\right)\right.\\ &\quad\left.+K_P\left(\alpha_h\right)\left(q_d(t)-q(t)\right)+K_d\left(\alpha_h\right)\left(\dot{q}_d(t)-\dot{q}(t)\right)\right]\end{aligned} \tag{7}$$

The stiffness variation in the smart chain structure with a 40-kg weight was evaluated (movie S8), and the wheelchair system effectively overcame the obstacle by changing the state of the wheel (Fig. 7C and movie S9). Using the wheelchair system, driving speed and performance were assessed in an atypical outdoor environment (movies S10 and S11), and the state transition of the wheel in real time was demonstrated; notably, the wheelchair system successfully overcame the obstacle (Fig. 7D and Movie 1).

DISCUSSION

Here, we presented a variable-stiffness wheel inspired by the surface tension of liquid. We established a variable-stiffness mechanism by controlling the tension of the wire spoke structure on the smart chain structure. We demonstrated the feasibility of the developed wheel by applying it to a four-wheeled vehicle and a

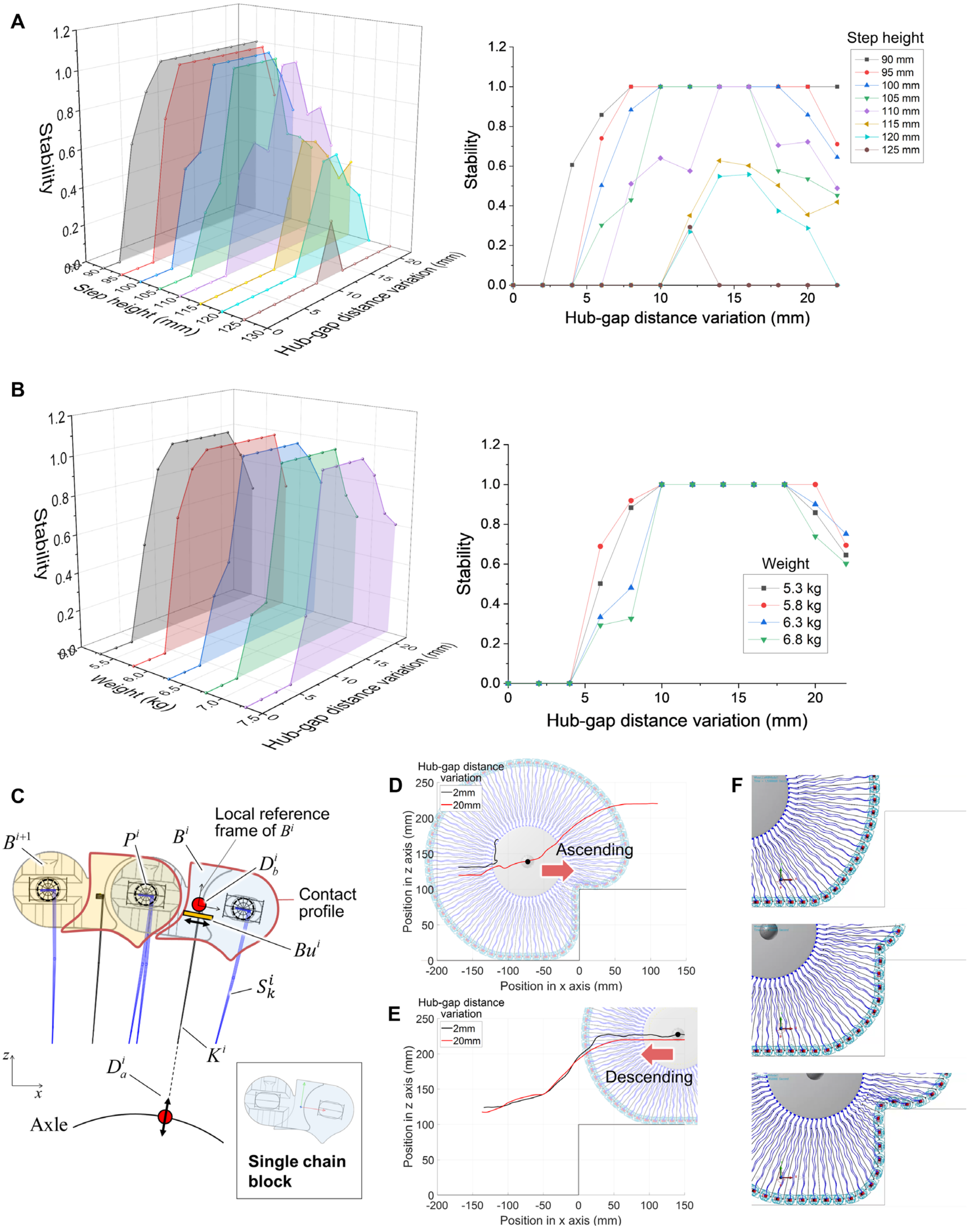

Fig. 6. Evaluation of the ability to overcome obstacles and simulation results. (**A**) Stability when overcoming obstacles considering the hub-gap distance variation and step height. (**B**) Stability when overcoming obstacles considering the hub-gap distance variation and weight applied to the wheel. (**C**) Description of the morphing-wheel simulation model. The trajectory of the wheel center based on the hub-gap distance variation for (**D**) ascending and (**E**) descending motions in the numerical simulation model. (**F**) Sequential deformation shape in the simulation.

two-wheeled wheelchair system. The wheel could overcome irregularly shaped rocks and steps that were 1.2 times higher than the wheel radius by changing its shape according to the target object through real-time state transition. However, noise and energy efficiency could not be evaluated in this study because the fabrication process used in this research was not automated or stabilized. Dust and particles can enter the areas between the smart chain blocks and cause damage to the wheel. Therefore, a wheel cover structure will be added in future research to encapsulate the developed wheel, similar to a typical tire structure. In addition, the smart chain block made of an acrylonitrile-butadiene-styrene (ABS) material will be replaced with one fabricated from thermoplastic polyurethane, and the current wire spoke structure will be modified to one with a thicker radius to enhance durability. Also, a nonlinear-based finite element analysis simulation will be developed to predict deformation characteristics of the soft supporting structure more accurately, with the goal of achieving a more precise prediction of the operating characteristics of the entire wheel structure. This study demonstrates real-time stiffness variation at the scale of the actual wheels used for a wheelchair, suggesting broader common applications in wheel-based robots and transportation systems for efficient driving on rough terrain.

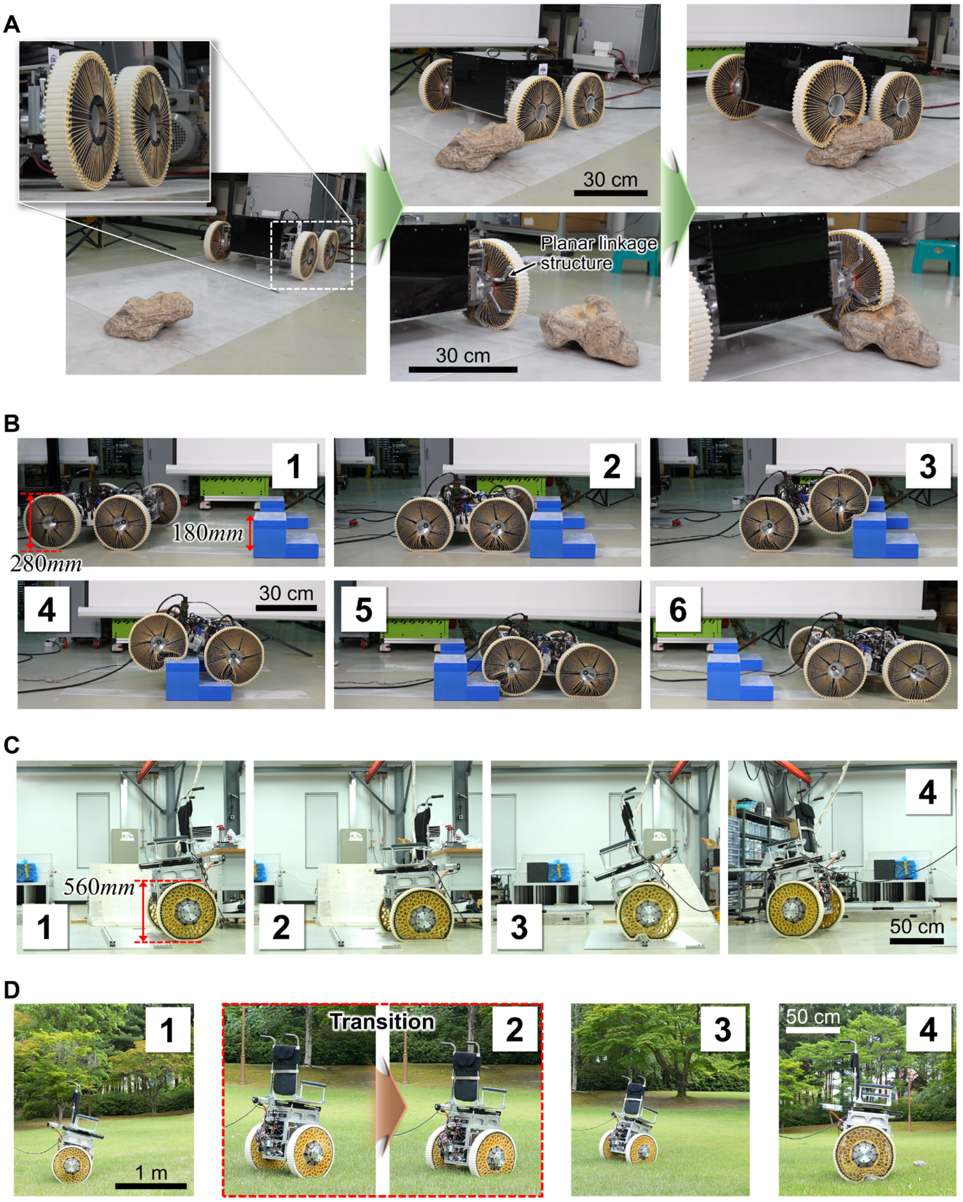

Fig. 7. Evaluation of wheel characteristics based on the surface tension. Demonstration of a four-wheeled vehicle overcoming a (**A**) rock and a (**B**) 180-mm step-shaped obstacle. Demonstration of a two-wheeled wheelchair system overcoming a (**C**) square obstacle and a (**D**) rock.

MATERIALS AND METHODS

Fabrication of the wheel

The smart chain block was fabricated with a three-dimensional (3D) printer (F370 Stratasys Inc.) with ABS (ABS-M30). Each chain block was connected by an aluminum rod with a radius of 2 mm. A sponge structure and a honeycomb structure were used as the soft supporting structure. The modulus of each sponge was measured (fig. S2). The honeycomb structure was fabricated with a 3D-printed mold (ABS-M30) and with liquid urethane rubber (Vytaflex 60, Smooth-On Inc.). The detailed fabrication process is described in figs. S34 and S35.

The material used for the wire spoke structure was Kevlar fiber with a thickness of 2 mm. For the small-sized wheel that was applied to the four-wheeled vehicle, the diameter of the wheel was 300 mm, and the width was 40 mm. For the large wheel that was applied to the wheelchair system, the wheel diameter was 560 mm, and the width was 90 mm.

Experimental setup

To evaluate the basic characteristics of the wheel, the load cell at the indenter was used to measure the reaction force of the wheel, and the other load cell at the hub structure was used to measure the required force to maintain the desired hub-gap distance (Fig. 4A). The two load cells (CSBA-50 L, CAS Ins.) at the hub structure and one load cell (CSBA-50 L, CAS Ins.) at the indenter were used to measure force. A laser displacement sensor (ODSL 96B M, Leuze) was used to measure the positions of the indenter and hub structure. The data were collected with the NI DAQ module (cDAQ-9172, NI-9215, National Instruments) and LabVIEW software. For the experiment in the flat-ground–condition case, an indenter with a square surface at the bottom with a length of 200 mm and a width of 40 mm was used.

The experimental system for evaluating the wheel was developed as shown in Fig. 5. A rail on which the wheel could move freely in the x-axis (forward) and z-axis (vertical) directions was

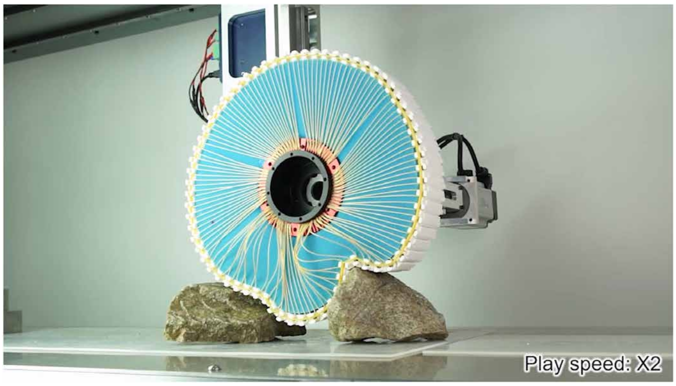

Movie 1. Demonstration of a vehicle with a variable-stiffness–morphing wheel. In a field demonstration, the mechanism realized stiffness variation based on variable surface tension.

installed in the system, and two motors that rotate the wheel and change the hub-gap distance were installed as the only parts of the wheel requiring power. The position of each smart chain block and the trajectory of the wheel were analyzed with image tracking software (ProAnalyst, Xcitex).

Configuration of the vehicle system

For the four-wheeled vehicle system, each wheel was actuated by using two motors: a motor (Maxon 488607 BLDC Motor) to rotate the wheel and a motor (Maxon 647692 BLDC Motor) to vary the hub-gap distance. The detailed configuration is shown in fig. S25. In the case of the two-wheeled wheelchair system, each wheel was actuated by using a motor (Komotek KAND-15DF3N2 AC Servo Motor) to rotate the wheel and a motor (Komotek KAFZ-06D) to change the hub-gap distance. A balancing algorithm was implemented with a controller. The detailed configuration and balancing algorithm are described in Supplementary Methods and figs. S29 to S32.

Statistical analysis

We used mean values ($\pm$ SD) for Fig. 2E and figs. S16 and S27 ($n = 5$ for each experimental condition) and for Figs. 2 (F and G) and 4 (E and H) and figs. S3, S14, and S15 ($n = 3$ for each experimental condition). Linear fitting equations and plots in Fig. 4 (C and D) were calculated and drawn using Origin 2023b.

Supplementary Materials

The PDF file includes:

Methods
Figs. S1 to S35
Table S1
References (*42*, *43*)

Other Supplementary Material for this manuscript includes the following:

Movies S1 to S11
MDAR Reproducibility Checklist

REFERENCES AND NOTES

1. F. Rubio, F. Valero, C. Llopis-Albert, A review of mobile robots: Concepts, methods, theoretical framework, and applications. *Int. J. Adv. Robot. Syst.* **16**, 10.1177/1729881419839596 (2019).
2. A. J. Ijspeert, Biorobotics: Using robots to emulate and investigate agile locomotion. *Science* **346**, 196–203 (2014).
3. R. A. Lindemann, C. J. Voorhees, "Mars Exploration Rover mobility assembly design, test and performance" in *2005 IEEE International Conference on Systems, Man and Cybernetics* (IEEE, 2005), vol. 1, pp. 450–455.
4. D. Kim, H. Hong, H. S. Kim, J. Kim, Optimal design and kinetic analysis of a stair-climbing mobile robot with rocker-bogie mechanism. *Mech. Mach. Theory.* **50**, 90–108 (2012).
5. K. Lim, S. Ryu, J. H. Won, T. Seo, A modified rocker-bogie mechanism with fewer actuators and high mobility. *IEEE Robot. Autom. Lett.* **7**, 8752–8758 (2022).
6. A. Suresh, N. Ajithkumar, S. T. Kalathil, A. Simon, V. J. Unnikrishnan, D. P. Mathew, P. Basil, K. Dutt, G. Udupa, C. M. Hariprasad, "An advanced spider-like rocker-bogie suspension system for Mars exploration rovers" in *Robot Intelligence Technology and Applications 4: Results from the 4th International Conference on Robot Intelligence Technology and Applications* (Springer, 2017), pp. 423–447.
7. L. Bruzzone, G. Quaglia, Review article: Locomotion systems for ground mobile robots in unstructured environments. *Mech. Sci.* **3**, 49–62 (2012).
8. L. Bruzzone, S. E. Nodehi, P. Fanghella, Tracked locomotion systems for ground mobile robots: A review. *Machines* **10**, 648 (2022).
9. C. Yang, K. Yuan, Q. Zhu, W. Yu, Z. Li, Multi-expert learning of adaptive legged locomotion. *Sci. Robot.* **5**, eabb2174 (2020).
10. J. Lee, J. Hwangbo, L. Wellhausen, V. Koltun, M. Hutter, Learning quadrupedal locomotion over challenging terrain. *Sci. Robot.* **5**, eabc5986 (2020).
11. T. Miki, J. Lee, J. Hwangbo, L. Wellhausen, V. Koltun, M. Hutter, Learning robust perceptive locomotion for quadrupedal robots in the wild. *Sci. Robot.* **7**, eabk2822 (2022).
12. S. Seok, A. Wang, M. Y. Chuah, D. Otten, J. Lang, S. Kim, "Design principles for highly efficient quadrupeds and implementation on the MIT Cheetah robot" in *2013 IEEE International Conference on Robotics and Automation* (IEEE, 2013), pp. 3307–3312.
13. H.-W. Park, P. M. Wensing, S. Kim, Jumping over obstacles with MIT Cheetah 2. *Robot. Auton. Syst.* **136**, 103703 (2021).
14. R. Playter, M. Buehler, M. Raibert, "BigDog" in *Unmanned Systems Technology VIII* (SPIE, 2006), vol. 6230, pp. 896–901.
15. M. Raibert, K. Blankespoor, G. Nelson, R. Playter, Bigdog, the rough-terrain quadruped robot. *IFAC Proc. Vol.* **41**, 10822–10825 (2008).
16. Boston Dynamics, Spot - The agile mobile robot; https://bostondynamics.com/products/spot.
17. F. L. Moro, A. Spröwitz, A. Tuleu, M. Vespignani, N. G. Tsagarakis, A. J. Ijspeert, D. G. Caldwell, Horse-like walking, trotting, and galloping derived from kinematic Motion Primitives (kMPs) and their application to walk/trot transitions in a compliant quadruped robot. *Biol. Cybern.* **107**, 309–320 (2013).
18. Boston Dynamics, Atlas and beyond: The world's most dynamic robot; https://bostondynamics.com/atlas.
19. I.-W. Park, J.-Y. Kim, J. Lee, J.-H. Oh, "Mechanical design of humanoid robot platform KHR-3 (KAIST humanoid robot 3: HUBO)" in *5th IEEE-RAS International Conference on Humanoid Robots, 2005* (IEEE, 2005), pp. 321–326.
20. J. Carpentier, S. Tonneau, M. Naveau, O. Stasse, N. Mansard, "A versatile and efficient pattern generator for generalized legged locomotion" in *2016 IEEE International Conference on Robotics and Automation (ICRA)* (IEEE, 2016), pp. 3555–3561.
21. S. Shigemi, "ASIMO and humanoid robot research at Honda" in *Humanoid Robotics: A Reference*, A. Goswami, P. Vadakkepat, Eds. (Springer, 2019), pp. 55–90.
22. T. Fukuda, P. Dario, G.-Z. Yang, Humanoid robotics—History, current state of the art, and challenges. *Sci. Robot.* **2**, eaar4043 (2017).
23. Tesla, Tesla bot update; https://youtu.be/XiQkeWOFwmk?si=fxn9E-6txpheq0hm.
24. G. Dudek, M. Jenkin, *Computational Principles of Mobile Robotics* (Cambridge Univ. Press, 2010).
25. V. Kubelka, M. Reinstein, T. Svoboda, Tracked robot odometry for obstacle traversal in sensory deprived environment. *IEEE ASME Trans. Mechatron.* **24**, 2745–2755 (2019).
26. M. Lauria, Y. Piguet, R. Siegwart, "Octopus: An autonomous wheeled climbing robot" in *Proceedings of the Fifth International Conference on Climbing and Walking Robots (CLAWAR'02)* (2002), pp. 315–322.
27. F. Michaud, D. Letourneau, M. Arsenault, Y. Bergeron, R. Cadrin, F. Gagnon, M.-A. Legault, M. Millette, J.-F. Paré, M.-C. Tremblay, Multi-modal locomotion robotic platform using leg-track-wheel articulations. *Auton. Robots* **18**, 137–156 (2005).
28. S. Shrivastava, A. Karsai, Y. O. Aydin, R. Pettinger, W. Bluethmann, R. O. Ambrose, D. I. Goldman et al., *Sci. Robot.* **5**, eaba3499 (2020).
29. Y. Deng, Z. Wang, H. Shen, J. Gong, Z. Xiao, A comprehensive review on non-pneumatic tyre research. *Mater. Des.* **227**, 111742 (2023).
30. Y. Zhao, X. Du, F. Lin, Q. Wang, H. Fu, Static stiffness characteristics of a new non-pneumatic tire with different hinge structure and distribution. *J. Mech. Sci. Technol.* **32**, 3057–3064 (2018).
31. L. Zhu, T. Xu, X. Liu, M. Wu, X. Zhou, F. Gao, Test and simulation study on the static load and pure longitudinal slip characteristics of non-pneumatic tire. *Machines* **11**, 86 (2023).
32. Z. Zhang, H. Fu, Q. Zhao, D. Tan, K. Yang, Pattern design and performance analysis of a flexible spoke bionic non-pneumatic tire. *J. Braz. Soc. Mech. Sci. Eng.* **43**, 1–11 (2021).
33. B. Bras, A. Cobert, Life-cycle environmental impact of Michelin Tweel tire for passenger vehicles. *SAE Int. J. Passeng. Cars-Mech. Syst.* **4**, 32–43 (2011).

34. Michelin, Michelin Uptis; https://michelinmedia.com/michelin-uptis.
35. H. Fu, X. Liang, K. Chen, Y. Wang, Z. Xiao, Study on key mechanical properties of the flexible spoke non-pneumatic tire considering thermo-mechanical coupling. *Adv. Eng. Softw.* **173**, 103281 (2022).
36. W. Xiao, Y. Zhang, Design of manned lunar rover wheels and improvement in soil mechanics formulas for elastic wheels in consideration of deformation. *J. Terramech.* **65**, 61–71 (2016).
37. G. Zambelli, "Research of shape memory alloy wheels for Mars rovers," thesis, Tampere University of Applied Sciences, Tampere, Finland/Polytechnic University of Catalonia, Catalonia, Spain (2021).
38. D.-Y. Lee, J.-K. Kim, C.-Y. Sohn, J.-M. Heo, K.-J. Cho, High–load capacity origami transformable wheel. *Sci. Robot.* **6**, eabe0201 (2021).
39. J. Berre, F. Geiskopf, L. Rubbert, P. Renaud, "Origami-inspired design of a deployable wheel" in *New Advances in Mechanisms, Mechanical Transmissions and Robotics: MTM & Robotics 2020* (Springer, 2021), pp. 114–126.
40. S. M. Felton, D.-Y. Lee, K.-J. Cho, R. J. Wood, "A passive, origami-inspired, continuously variable transmission", in *2014 IEEE International Conference on Robotics and Automation (ICRA)* (IEEE, 2014), pp. 2913–2918.
41. C. Grand, P. Bidaud, N. Jarrassé, "Innovative concept of unfoldable wheel with an active contact adaptation mechanism" in *Proceedings of 12th World Congress in Mechanism and Machine Science* (IFToMM, 2007), pp. 1225–1232.
42. J. Shen, Y. M. Xie, X. Huang, S. Zhou, D. Ruan, Mechanical properties of luffa sponge. *J. Mech. Behav. Biomed. Mater.* **15**, 141–152 (2012).
43. M. Kim, J. Park, D. I. Park, C. Park, J. Cheong, Dynamic inversion based real-time trajectory planning method for wheeled inverted pendulum using asymptotic expansion technique. *IEEE Access* **11**, 94805–94821 (2023).

Acknowledgments: We thank J.-H. Lee and J.-W. Bae (Korea Institute of Materials Convergence Technology) for advising on appropriate materials and fabricating the polymer structures, J.-C. Kim (Department of Thermal Energy Solutions, Korea Institute of Machinery and Materials) for advising on the surface tension model of liquid and wheel mechanism, and M.-S. Bae (DyenceTech) for detailed modeling and assembly of the two-wheeled mobile system. **Funding:** This research was supported by a grant of the major project of the Korea Institute of Machinery and Materials (project ID NK244F). **Author contributions:** J.-Y.L. designed and built the smart chain block, performed the experiments, and wrote the manuscript; S.H. developed the simulation to evaluate the wheel characteristics; M.K. developed the control algorithm of the two-wheeled system; Y.-S.S. performed the experiment and analyzed the data; J.P. developed the two-wheeled and four-wheeled platform system hardware; D.I.P. advised on the simulation of the wheel; C.P. directed the project; H.S. developed the electrical system of the platform; J.L. assisted in the simulation of the wheel deformation; H.-S.K. designed the wire tension variation module at the large scale; J.B. assisted the design of the tension variation mechanism; H.R. edited the manuscript; J.-G.K. directed the simulation to evaluate the wheel characteristics; J.C. directed the control algorithm for the two-wheeled system; and S.-H.S. created, designed, and developed the wheel mechanism, performed the experiments, directed the project, and wrote and edited the manuscript. **Competing interests:** S.-H.S., J.-Y.L., J.P., D.I.P., C.P., and H.-S.K. are inventors on the patent application (US 18/258,035, EPO. 22739656.1, JP. 2023-537321, CN. 22739656.1, and PCT/KR2022/000537) submitted by the Korea Institute of Machinery and Materials that covers the design of the wheel structure. **Data and materials availability:** All data needed to support the conclusions of this manuscript are included in the main text or Supplementary Materials. The related data, files, and code for this study have been deposited in Dryad at https://doi.org/10.5061/dryad.kwh70rzd7 and in Zenodo at https://doi.org/10.5281/zenodo.12702711.

Submitted 5 October 2023
Accepted 16 July 2024
Published 14 August 2024
10.1126/scirobotics.adl2067

Science Robotics

Variable-stiffness–morphing wheel inspired by the surface tension of a liquid droplet

Jae-Young Lee, Seongji Han, Munyu Kim, Yong-Sin Seo, Jongwoo Park, Dong Il Park, Chanhun Park, Hyunuk Seo, Joonho Lee, Hwi-Su Kim, Jeongae Bak, Hugo Rodrigue, Jin-Gyun Kim, Joono Cheong, and Sung-Hyuk Song

Sci. Robot. **9** (93), eadl2067. DOI: 10.1126/scirobotics.adl2067

Editor's summary
With their speed and low cost of transport, wheels are a favorable choice of locomotion for robots. However, wheels cannot easily navigate over large obstacles, restricting their use in certain environments. Here, Lee *et al.* developed a wheel with adjustable stiffness that can be changed in real time, taking on a rigid, circular shape on flat ground and a soft, deformable shape for rolling over large obstacles. A smart chain structure along the outside of the wheel connects to a center hub via a spoke structure. The tension in the spokes can be adjusted to adapt the wheel stiffness, allowing the wheels to move across a variable terrain. The wheel capabilities are demonstrated in a four-wheeled vehicle and a two-wheeled wheelchair system. —Melisa Yashinski

Science Robotics (ISSN 2470-9476) is published by the American Association for the Advancement of Science. 1200 New York Avenue NW, Washington, DC 20005. The title *Science Robotics* is a registered trademark of AAAS.